The Mechanism of Rapid and Green Metal-Organic Framework Synthesis by In Situ Spectroscopy and Diffraction

Article

The Mechanism of Rapid and Green Metal−Organic Framework Synthesis by *In Situ* Spectroscopy and Diffraction

Ilia Kochetygov,* Luca Maggiulli, Marco Ranocchiari, and Davide Ferri*

Read Online

ACCESS | Metrics & More | Article Recommendations | Supporting Information

ABSTRACT: Room-temperature aqueous synthesis provides facile access to metal−organic frameworks (MOFs) through green routes, avoiding the use of toxic solvents at high temperatures that are typical for common solvothermal MOF synthesis routes. Nevertheless, mechanisms of green aqueous MOF syntheses remain unexplored, hindering their further development. In this work, we for the first time report a comprehensive investigation of the synthesis of a MOF, Zn-MOF-74 (also known as CPO-27-Zn), in aqueous phase at room temperature. Using a unique combination of *in situ* infrared spectroscopy (IR) and high-energy X-ray diffraction (XRD), we reveal mechanistic insights into the fast synthesis (2−10 min) of Zn-MOF-74 from different sources, zinc acetate, and zinc perchlorate, at six different temperatures from 5 to 40 °C. A 5-fold acceleration was observed when using the noncoordinating perchlorate ion, making it an alternative precursor to decrease synthesis time. Furthermore, a correlation between IR and XRD data was established, allowing to monitor nucleation and growth processes individually with both techniques. Last, the particle size and shape distribution was linked to the differences in mechanistic kinetic parameters, allowing for their control by the choice of synthesis temperature and precursors.
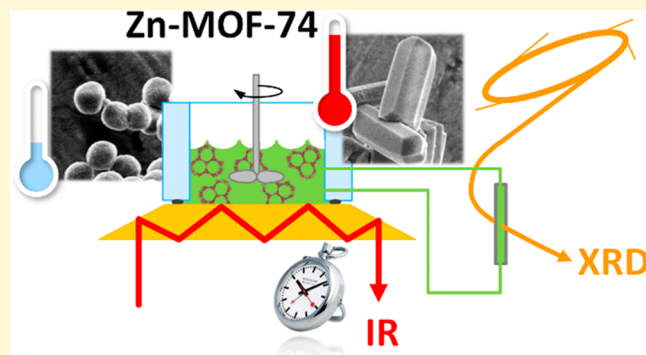
INTRODUCTION

Metal−organic frameworks (MOFs) are state-of-the-art porous materials[1] that display promising performance in separations,[2,3] gas storage,[4] catalysis,[5,6] and sensing.[7] Being constructed by a combination of metal clusters or secondary building units (SBUs) interlinked by organic ligand molecules,[8,9] they offer unprecedented tunability that enables tailoring MOFs to specific application requirements.[10] After more than 30 years of discovery and development, MOFs are starting to find industrial use, as recently exemplified by CALF-20, which has exceptional carbon capture performance and as of today is produced at a several hundred tons per year scale.[11,12] The success of MOF implementation depends on a combination of factors, of which the ease of synthesis and scalability stand out as they largely control the cost-effectiveness and viability of the material.[13−16]

Besides the discovery of novel MOF structures and compositions, synthesis remains a leading topic in MOF chemistry. One of the most promising approaches to synthesizing MOFs is the recently reported green, aqueous, room-temperature synthesis involving the reaction of a metal salt, such as nitrate or acetate, with a sodium salt of the ligand, producing within several minutes or hours the MOF and only the sodium salt of a common anion as the byproduct.[17−19] Avoiding the drawbacks of solvothermal synthesis routes, such as the use of toxic or harmful solvents at high temperatures (up to 250 °C) coupled with reaction times of several days,[20] the green aqueous method attracts attention due to its simplicity and sustainable

nature.[21] However, it is not universally applicable to many MOF families, while the solvothermal methods are general in character.[22]

The puzzling specificity of aqueous synthesis prompts mechanistic investigations of its nature. While numerous works have investigated MOF formation in solvothermal[23−25] and mechanochemical[26] conditions using a number of physicochemical methods and advanced density functional theory (DFT) simulations, strikingly, to the best of our knowledge, there is no report yet on the mechanism of MOF synthesis in the aqueous phase. Understanding such synthesis is a key aspect because it not only contributes to the fundamental knowledge of MOF formation. It also yields crucial insights into the underlying mechanisms governing MOF synthesis enabling further development and providing guidance for the synthesis of innovative functional materials. For instance, in mechanistic studies of the solvothermal syntheses, three key steps in the mechanism of MOF formation were determined, namely, solution-based formation of MOF prebuilding blocks, followed

by nucleation and further crystal growth.[25] A subtle interplay among the parameters of these three steps determines the overall MOF production rate, the presence of defects, the morphology, and the success of synthesis.[27]

It must be noted, however, that studying aqueous syntheses poses a notable challenge due to their prompt nature, with reactions completing within minutes. For successful kinetic modeling, this requires data collection with second and subsecond time resolution that is not needed for other synthesis approaches. We believe this also contributes significantly to the evidence that there are no known studies on aqueous room-temperature MOF synthesis mechanism so far.

In this work, we studied the synthesis of Zn-MOF-74 (also known as CPO-27-Zn)[17] in the aqueous phase at room temperature using a combination of *in situ* attenuated total reflectance infrared spectroscopy (ATR-IR) and high-time resolution X-ray diffraction (XRD) for the first time. These techniques were chosen carefully to complement each other, as the ATR-IR is sensitive to the molecular structure change in both solid and liquid phases, while the XRD provides specific information on crystalline phase of the material such as unit cell dimensions and crystalline domain size. Furthermore, both techniques provide suitable time resolution for studying the fast aqueous MOF synthesis. Developing a new experimental setup and combining both techniques, supplemented by in-depth data analysis by multivariate curve resolution (MCR) and time-dependent peak deconvolution, enabled unique mechanistic insights into MOF formation during fast aqueous reactions. Importantly, a correlation between IR (peak width) and XRD (probability of nucleation from a kinetic model) is established, allowing to use a widely available ATR-IR technique for monitoring nucleation and growth processes in the synthesis separately. The results are further completed by a comprehensive particle size distribution analysis where the dependency of crystal size, shape, and aspect ratio of the resulting Zn-MOF-74 particles on the synthetic conditions and nucleation and growth kinetic parameters is clearly established. Based on the *in situ* spectroscopic evidence, we propose an underlying precursor- and temperature-dependent mechanism and new protocols for rapid and high-quality Zn-MOF-74 synthesis.

■ EXPERIMENTAL SECTION

General Notes. All chemicals were used as received from commercial suppliers. Milli-Q water was used for MOF synthesis, while distilled water was used for washing.

Attenuated Total Reflectance (ATR) IR Spectroscopy. A custom ATR-IR batch reactor cell was installed in the Thermo Fischer Nicolet 6700 spectrometer controlled by Omnic 8.3 software and equipped with a liquid N_2-cooled MCT detector. The cell consisted of a stainless steel cylindrical body (internal volume of 20 mL) and a stainless steel lid with various apertures to enable gas/liquid injection and withdrawal, stirring, pH measurement, etc. The temperature of the cell body was controlled using a recirculating thermostat (Julabo F32 CH) and water as the medium. A ZnSe (30°, 50 × 20 × 2 mm) internal reflection element (IRE) served as the batch reactor bottom and allowed probing the reaction mixture by infrared light. The IRE was deposited in a groove of the horizontal stainless steel cell bottom plate onto which the cell body was screwed and was sealed using a Viton O-ring. An overhead mechanical stirrer (IKA-Werk RE 162A) equipped with a PTFE turbine blade (Bohlender C482−12) inserted through the cell lid ensured vigorous and powerful stirring (500 rpm) that proved essential to avoid sedimentation of the solid, which could disturb the homogeneous distribution of the contents of the reactor and make the IR signal nonrepresentative of the whole reaction mixture.

General Protocol for *In Situ* ATR-IR Experiments. Zinc acetate and zinc perchlorate solutions were prepared by dissolving 0.5615 g $Zn(OAc)_2 \cdot 2H_2O$ (2.558 mmol, 2 equiv) or 0.9526 g $Zn(ClO_4)_2 \cdot 6H_2O$ (2.558 mmol, 2 equiv) in 7 mL of Milli-Q H_2O directly in the *in situ* ATR-IR cell. The ligand solution was prepared by dissolution of 0.2533 g of 2,5-dihydroxyterephthalic acid (H_4dobdc, 1.278 mmol, 1 equiv) and 0.513 mL of 10 N NaOH (5.130 mmol, 4 equiv) in 7 mL of Milli-Q H_2O inside a capped 10 mL syringe. Ultrasound was employed to ensure full dissolution of the ligand (no visible solid/opacity) and to obtain a transparent brown solution. The syringe with the ligand solution was submerged in the thermostat bath for ca. 30 min to allow for thermal equilibration with the zinc solution, and IR data collection was started at a time resolution of 6.15 s and a spectral resolution of 4 cm^{-1}. The ligand solution was added to the zinc solution under vigorous stirring, in one shot. Stirring and data collection continued for 2 h, whereupon the reaction mixture was subjected to centrifugation (3 min, 4,000 rpm) and subsequent washings with water (3 × 50 mL) and methanol (3 × 50 mL). The sample was then submerged in 50 mL of methanol for 1 week while changing the solvent every 24 h. Finally, the material was vacuum-dried overnight at room temperature and analyzed as described below.

X-Ray Diffraction (XRD) Measurements. In-house powder XRD measurements were performed on a Bruker D8 Advance diffractometer operating in Bragg−Brentano geometry using CuKα radiation. Diffractograms were collected from 4 to 40° 2θ with a step size of 0.02° and 1 s measurement time per step.

In situ XRD measurements were performed in transmission geometry at the ID15A beamline of the European Synchrotron Radiation Facility (ESRF, Grenoble, France) at an X-ray wavelength of λ = 0.193725 Å. Data were collected at a time resolution of 50−100 ms using a DECTRIS Pilatus3 X CdTe 2 M detector. The same reactor cell used for the ATR-IR experiments was modified to replace the bottom part including the ZnSe crystal with a stainless steel plate. The setup was further adapted to include a sample loop enabling online monitoring of the diffraction signal of the reaction mixture through a Kapton capillary. The protocol for the *in situ* measurements was modified as in the following:

- Instead of manual addition, the ligand solution was added via a remotely controlled peristaltic pump.

- A second peristaltic pump was connected in a loop that collected the reactant slurry from the bottom of the reactor, passed it through the X-ray beam in a Kapton capillary (1.2 mm internal diameter), and returned it to the reactor. In each experiment, this pump was remotely turned on 3 s after the addition of the ligand was finished.

BET Measurements. Nitrogen adsorption isotherms at 77 K were measured on a Micromeritics 3Flex instrument. Prior to measurements, samples were activated using a VacPrep 061 degassing station at 250 °C (5 °C min^{-1} ramp from room temperature to 250 °C followed by 12 h plateau at 250 °C and natural cooling to room temperature). Data in the p/p_0 range 0.003−0.01 were used for BET calculations.

MCR Analysis and Background Subtraction of the ATR-IR Data. In order to extract the quantitative information on the species evolution as well as their pure spectra, we employed the multivariate curve resolution-alternating non-negatively constrained least-squares (MCR-AR-NNLS) method.[28] This method combined with the principle component analysis (PCA) allows us to estimate the number of individual components in the data set and to decompose the full measurement into a set of components and their time profiles. The data were background-subtracted using the Whittaker smoothing asymmetric least-squares approach as implemented in the pybaselines package.[29] Then, Python scripts for the analysis were adapted from the original reference[28] to obtain the MCR analysis results.

FTIR Peak Fitting Details. The two peaks of the ATR-IR spectra in the region from 1385 to 1452 cm^{-1} were fitted with a Pseudo-Voigt profile as implemented in the LMFIT Python package.[30] Prior to the fitting, the data were background-subtracted using the Whittaker smoothing asymmetric least-squares approach as implemented in the pybaselines package.[29] During the peak fitting, all the parameters,

namely amplitude, FWHM, fraction, and center, were free to refine independently.

***In Situ* XRD Data Analysis.** After the raw data integration, the powder patterns with 50 (zinc perchlorate data sets) or 100 ms (zinc acetate data set) time resolution were sequentially analyzed by fitting selected diffraction peaks with a Pseudo-Voigt profile as implemented in the LMFIT Python package.[30] The simulated pattern for results comparison and peak indexing was produced and indexed in Vesta[31] from the ORIVOC CCDC entry.[32] Prior to the fitting, the data were background-subtracted using the LOESS algorithm as implemented in the pybaselines package.[29]

During the peak fitting, all the parameters, namely amplitude, FWHM, fraction, and center, were free to refine independently. For Gualtieri model fits, the peak amplitudes (which are proportional to the peak areas) of all the fitted peaks were first normalized, and then averaged to produce the value of α vs time to be used for the model fits.

Lattice Parameters Calculation. Using the peak position vs time values obtained from the peak fitting, d_{hkl} values vs time were calculated for all the fitted peaks. Then, at each time point, lattice parameters and their uncertainties were extracted by fitting (eq 1) for d_{hkl} in a hexagonal crystal system via the least-squares method in the LMFIT Python package.[30]

$$\frac{1}{d_{hkl}^2} = \frac{4}{3} \cdot \left(\frac{h^2 + hk + k^2}{a^2} \right) + \frac{l^2}{c^2} \qquad (1)$$

Williamson-Hall Analysis. Williamson-Hall analysis of the *in situ* XRD data was performed in the following manner. First, instrumental peak widths were obtained by fitting the CeO_2 standard. Next, instrumental peak width was extrapolated to lower 2θ values using a linear regression, and for each peak designated as $\beta_{standard}$, β_{total}, the contribution of the sample to the peak broadening was calculated as shown in eqs 2–4 below, where α is the Pseudo-Voigt fraction, β_G and β_L are Gaussian and Lorentzian contributions to the sample peak width. These calculations were done for each peak at each time point.

$$\beta_G = \sqrt{\beta_{total}^2 - \beta_{standard}^2} \qquad (2)$$

$$\beta_L = \beta_{total} - \beta_{standard} \qquad (3)$$

$$\beta_{sample} = \alpha\beta_L + (1 - \alpha)\beta_G \qquad (4)$$

Next, two sets of Williamson-Hall fits for peaks with l = 0 and l = −1 were performed at each time point, following linear regression shown in (5), where ε is strain, K = 0.89, λ is the X-ray radiation wavelength (0.193725 Å) and D is the crystalline domain size.

$$\beta_{sample}\cos(\theta) = 4\varepsilon\sin(\theta) + \frac{K\lambda}{D} \qquad (5)$$

Williamson-Hall analysis of the in-house XRD data of the synthesis products was performed in a similar fashion. Al_2O_3 NIST SRM 1976b was used as the standard, and all the peaks were fitted as Lorentzian profiles.

Particle Size and Shape Distribution Analysis. SEM images were obtained on a ZEISS Ultra-55 Scanning Electron Microscope at an accelerating voltage of 3 kV and a working distance of 10.8 mm using an Everhart-Thornley SE2 detector (Carl Zeiss) and analyzed using a web version of ImageJ (ij.imjoy.io) on a tablet.[33] Particles were outlined using a stylus, and their shapes were fitted by a minimal area rectangle. The widths and lengths of such rectangles correspond to the widths and lengths of particles. Hundreds of particles (Table S1) were analyzed for each sample (except $Zn(OAc)_2$ at 25 °C sample due to large crystal size and significant intergrowth) to accumulate representative statistics of their size distribution.

■ RESULTS AND DISCUSSION

***In Situ* Infrared Spectroscopy.** In order to study the ambient temperature synthesis of Zn-MOF-74 at a preparative scale using vibrational spectroscopy, we used a batch reactor cell

designed for attenuated total reflection infrared spectroscopy (ATR-IR, Figure S1-3).[34,35] The *in situ* ATR-IR spectra obtained under experimental conditions similar to those described by Garzon-Tovar et al.[17] using zinc acetate as the zinc source, were dominated by the spectrum of the acetate ion (Figure S4). Only the signals at 1240 ($\nu(C-O)$) and 1193 cm^{-1} ($\beta(C-H)$) were indicative of the formation of Zn-MOF-74 by comparison with the spectra of the starting materials and the end product (Figure S5).[36] To better visualize the underlying processes and bypass the disturbance by the acetate ion, difference spectra were calculated by subtracting the spectrum measured prior to the addition of the ligand solution from the subsequent spectra in the time series (Figure 1). In these spectra,
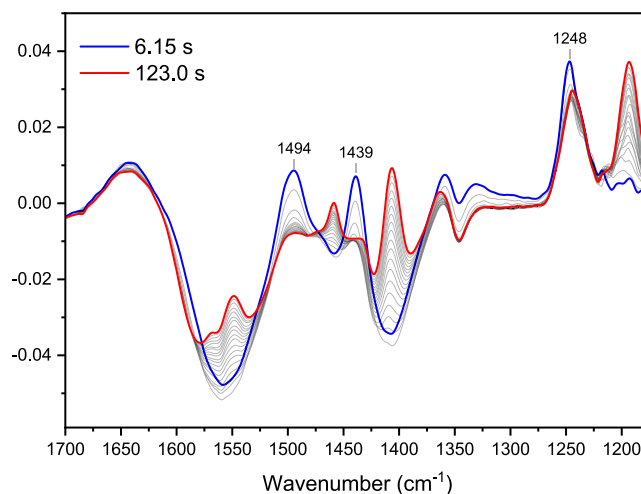

Figure 1. Difference *in situ* ATR-IR spectra obtained during Zn-MOF-74 synthesis with zinc acetate at 25 °C.

the signals of the acetate ion appear negative as the ligand consumes the zinc acetate. Additionally, new features were also evident at 1494 and 1439 cm^{-1} at the very early stages of the reaction, which disappeared gradually in favor of the MOF bands at 1549 ($\nu_{as}(C=O)$), 1406 ($\nu(C=C_{Ar})$) and 1193 ($\beta(C-H)$) cm^{-1} along time, suggesting formation of an intermediate species in the reaction mixture. The main MOF band growing at 1406 cm^{-1} also red-shifted gradually.

The appearance of the intermediate species prompted further investigation of its origin. Its three characteristic bands at 1494, 1439, and 1248 cm^{-1} matched neither the spectrum of the starting ligand that was added to the zinc acetate solution nor that of the zinc 2,5-dihydroxyterephthalate ($Zn(H_2dobdc)$), a 1D polymer previously reported as an intermediate in mechanochemical Zn-MOF-74 synthesis.[26] Thus, to understand the nature of the intermediate, it was desirable to extract its pure spectrum that could help with the identification. Efforts to analyze the data of Figure 1 by multivariate curve resolution (MCR)[37] to extract pure components in this reaction were unsuccessful, likely because of the strong overlap of the intense acetate peaks with the weak intermediate signal limiting the ability of MCR to detect the transient component.

The spectra obtained during the synthesis of Zn-MOF-74 with zinc acetate precursor were complex and did not allow extracting kinetic information on precursors, intermediate species, and product evolution as well as straightforward component identification, largely due to the broad acetate bands present in the spectra throughout the whole experiment. Based on the examination of the vibrational spectra of common
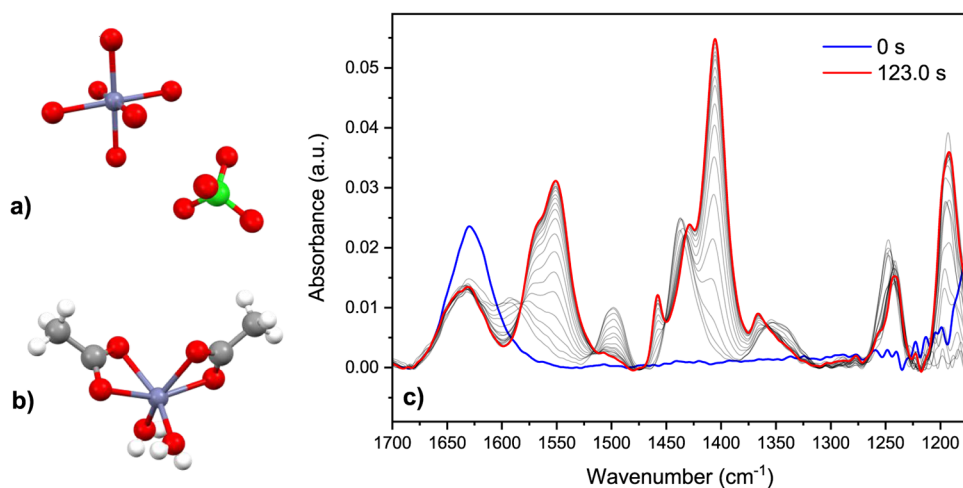
Figure 2. Crystal structures of (a) zinc perchlorate hexahydrate and (b) zinc acetate dihydrate. Atom colors: Zn, lavender; O, red; C, gray; Cl, green; H, white. H atoms are omitted in (a) for the sake of clarity. (c) *In situ* ATR-IR spectra obtained during Zn-MOF-74 synthesis with zinc perchlorate at 25 °C.
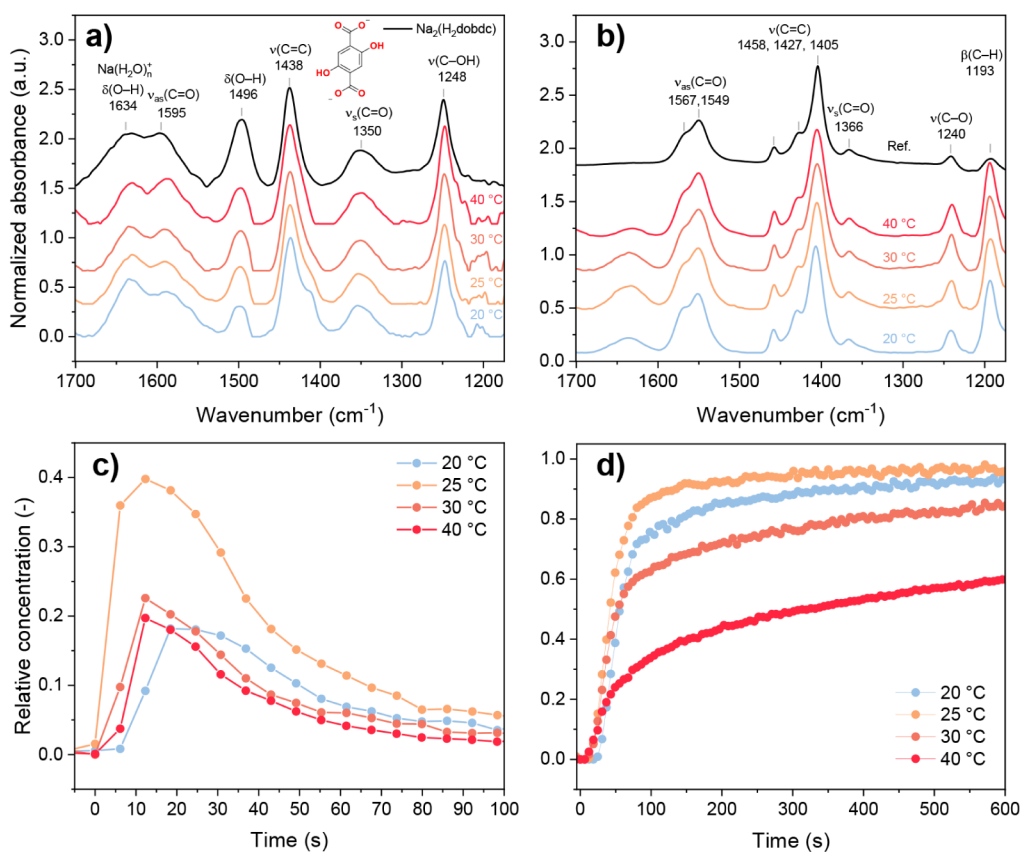

Figure 3. ATR-IR spectra of (a) intermediate and (b) product components obtained from MCR-AR-NNLS; relative concentration curves of (c) intermediate and (d) product at 20−40 °C. The top spectrum of panel (b) is the spectrum of the dry Zn-MOF-74 powder sample obtained from these syntheses.

anions and their coordinating ability, zinc perchlorate (Figure 2a) was selected as a substitute for zinc acetate (Figure 2b) to carry out the ATR-IR measurements and to identify the nature of the intermediate. The spectrum of zinc perchlorate aqueous solution is notably simpler, showing the $\delta(\text{O−H})$ mode of the water molecules coordinated to Zn^{2+} at 1630 cm^{-1} and the $\nu(\text{Cl−O})$ mode at 1134 cm^{-1} typical of noncoordinated

perchlorate ions but most importantly, no bands in the region of interest for MOF synthesis (Figure S6).[38]

The *in situ* ATR-IR spectra obtained during MOF synthesis with zinc perchlorate shown in Figure 2c (raw data in Figure S7) demonstrate a remarkable clarity compared to the data obtained with zinc acetate. Excluding the contribution of Zn- or Na-bound water at 1630 cm^{-1},[39] isosbestic points at 1582, 1516, and 1359 cm^{-1} indicate the presence of two interconverting species.

In the early stages of the experiment, the spectra exhibited the same bands of the intermediate species observed with zinc acetate at 1494 and 1248 cm^{-1}, but new intermediate bands became visible at 1437 and 1350 cm^{-1}, providing additional information on the nature of the intermediate species. The evolution of these signals and that of Zn-MOF-74 at 1406 cm^{-1} was free of interference and was further analyzed. From a qualitative vibrational spectroscopy perspective, the use of the perchlorate ion precursor did not change the result of the Zn-MOF-74 synthesis.

The improvement of the spectral quality with zinc perchlorate allows us to better understand the process of Zn-MOF-74 synthesis. Hence, *in situ* ATR-IR spectra were collected at different temperatures to evaluate the kinetic behavior of the components present in the reaction mixture and were analyzed by the multivariate curve resolution-alternating non-negatively constrained least-squares (MCR-AR-NNLS) method.[20] The results in Figure 3 and Figures S8−S11 show that the components in the reaction mixture were always the same from a spectroscopic point of view irrespective of temperature: zinc perchlorate, the intermediate species, and the product Zn-MOF-74.

To unveil the nature of the intermediate species, the pH of the reaction mixture was measured during the reaction at 25 °C using a pH probe inserted in the batch reactor to discover that it leveled off at a value of ca. 6.8 quickly after the addition of the ligand (Figure S12). In this pH range, the H$_4$dobdc ligand is 2-fold deprotonated and exists as a 2,5-dihydroxyterephthalate ion (H$_2$dobdc^{2-}), as established by pH-controlled experiments with the ligand (Figure S13). When an aqueous solution of H$_4$dobdc was prepared with two equivalents of sodium hydroxide, a spectrum of Na$_2$H$_2$dobdc was obtained, matching that of the intermediate species of Zn-MOF-74 synthesis (Figure 3a). Hence, the intermediate is the ligand that changes speciation upon the pH equilibration with the zinc salt solution. The starting solution of the ligand with four equivalents of NaOH does not possess the same spectrum, and at its pH (13) at least one hydroxyl group is expected to be deprotonated. Upon mixing with the acidic zinc perchlorate solution and given that the proton mobility is the highest among the reaction species,[40] the pH equilibrates faster than the MOF synthesis reaction proceeds leading to accumulation of the ligand as H$_2$dobdc^{2-} species in solution prior to their consumption to form the MOF. Therefore, we are able to provide molecular-level insights into the formation and existence of this intermediate molecular species of Zn-MOF-74 synthesis. The MCR component associated with the product obtained at different temperatures always displayed the same spectrum identical to that of pure Zn-MOF-74 in water (Figure 3b), except for the band at 1633 cm^{-1} belonging to the Na-bound water in the NaClO$_4$ byproduct of the synthesis. The kinetic curves of the intermediate species (Figure 3c) and of the product (Figure 3d) display typical behavior for their nature, with intermediate concentration peaking at around 10−20 s and product concentration displaying a sigmoidal curve. Within the time resolution of our experiments (6.15 s), the only visible difference among the experiments at different temperatures is a delayed maximum concentration of the intermediate species at 20 °C (18.45 s) compared to higher temperatures (12.3 s). The shoulder at ca. 1410 cm^{-1}, also visible in the spectra of the intermediate species (Figure 3a), does not belong to the H$_2$dobdc^{2-} anion. Close inspection of the data in Figure 2c revealed the emergence of a band in this region that intensified smoothly and shifted to lower

energy, eventually converging to the main band of the Zn-MOF-74 at 1405 cm^{-1} over the course of the experiment. Therefore, we were able to follow the evolution of the Zn-MOF-74 species from the beginning of the reaction. To better understand and quantify this, the two evolving peaks in the region 1450−1380 cm^{-1} were deconvoluted using time-resolved peak fitting with Pseudo-Voigt profiles as implemented in the LMFIT library (Figures S14 and S15)[30] so as to separate and track the evolution of Zn-MOF-74 in the early stages of synthesis. While it was already clear from the raw spectra that the peak red-shifted and stabilized with time, peak fitting was needed to uncover changes in the peak full width at half-maximum (FWHM). The FWHM passed through a maximum value after 20 s of reaction before decreasing to reach a stable value corresponding to that of the MOF product (Figure S15). This implies that the speciation of the system was the most complex at the beginning and comprised different molecular species and probably small MOF crystallites, which are all characterized by unique vibrational signatures of similar energy giving rise to the observed broad peak.

In Situ X-Ray Diffraction and Further Characterization.

We used time-resolved high-energy X-ray diffraction to unveil the evolution of the crystalline component within the mixture. It must be noted that the molecular intermediate observed by ATR-IR was silent in XRD as it is a part of liquid phase that lacks long-range order. The three main pieces of information extracted from the diffraction experiments were the time-dependent extent of crystallization (α), the FWHM of selected XRD peaks, and the lattice parameters a and c. In the Zn-MOF-74 synthesis using zinc perchlorate at 25 °C, several peaks of different Miller indices (Figures S16, S17) were selected for FWHM analysis. The temporal evolution of FWHM revealed a clear dependence on Miller indices. The peaks with index $l = 0$ displayed nearly no evolution in the noise-stabilized region (after ca. 10 s, Figure S18a), while the FWHM of the peaks with index $l = -1$ displayed an evident decrease over time after ca. 10−20 s (Figure S18b). To better understand the origin of this peak width evolution, a time-dependent Williamson-Hall analysis was performed to deconvolute the size and strain contributions to the FWHM (Figure S18, c−f).[41] The initial decrease of FWHM ($l = -1$) observed within 40 s can be attributed to the evolution of the size of the crystalline domains from ca. 50 to >200 nm (Figure S18d), above which XRD is insensitive to size changes.[42] The remaining peak width is explained by the residual strain in the material. For peaks with $l = 0$, there was no noticeable size evolution (Figure S18c), while the strain values were close to those of peaks with $l = -1$ (Figures S18e and Figure S18f). These results illustrate that the crystal growth during synthesis occurred along the c axis of the hexagonal $R\bar{3}$ cell of Zn-MOF-74. This observation is further corroborated by the temporal evolution of the lattice parameter values (Figure 4). The c parameter (Figure 4b) and XRD peak FWHM (Figure 4c) exhibited similar behavior, that is a decrease over time followed by stabilization after ca. 50 s. This could be related to the formation of a less efficiently packed MOF structure in the early stages of synthesis. The relative magnitude of change of 0.6% compared to only 0.04% for the a parameter (Figure 4b) also revealed that the c parameter was also more susceptible to structural changes during synthesis.

The last parameter derived from the XRD, α, bears information that can be extracted using the well-established Gualtieri model, eq 6,[43,44] namely the kinetic constants of MOF nucleation ($k_N = 1/a$) and growth (k_G), the type of nucleation
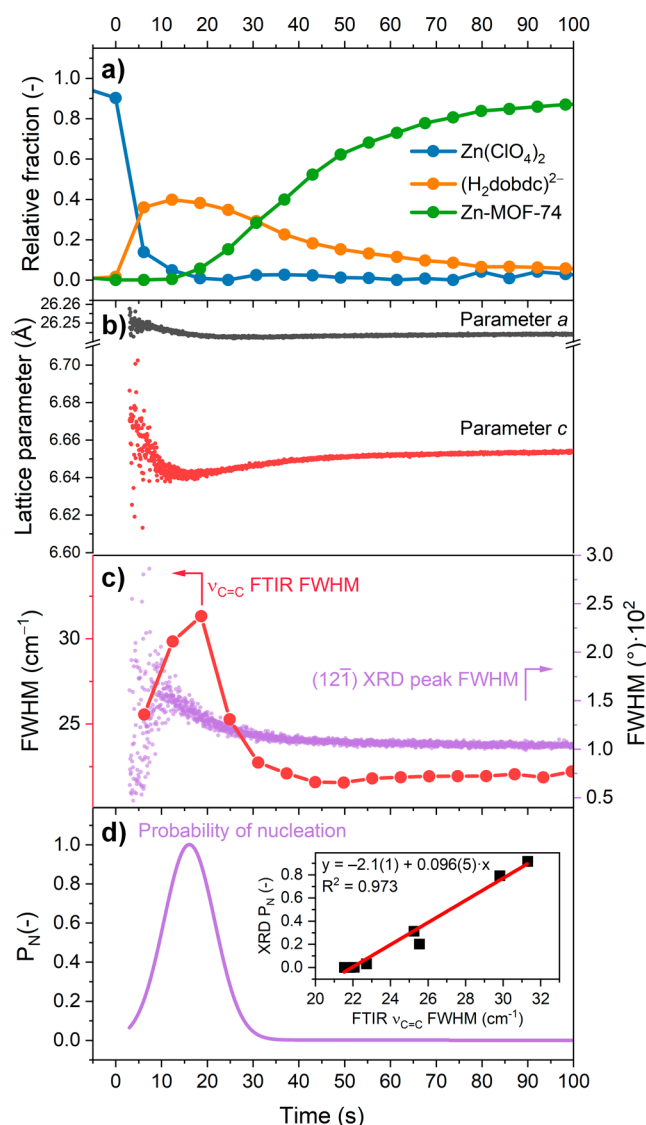
Figure 4. Parameters derived from *in situ* ATR-IR ((a) MCR relative fractions, (c) $\nu(C=C_{Ar})$ peak FWHM) and XRD ((b) lattice parameters a and c, (c) 12−1 peak FWHM and (d) probability of nucleation). The inset in (d) demonstrates the relation between P_N and $\nu(C=C_{Ar})$ peak FWHM.

(depending on the value of parameter b), and the probability of nucleation P_N, eq 7, at different time stages.

$$\alpha = \frac{1}{1 + e^{-\left(\frac{t-a}{b}\right)}} \cdot \left(1 - e^{-(k_g t)^n}\right) \tag{6}$$

$$P_N = e^{-(t-a)^2/2b^2} \tag{7}$$

The n parameter in eq 6 depends on the dimensionality of particle growth and can take values 1, 2, or 3 for 1D, 2D, or 3D growth, respectively. Fits with $n = 1, 2, 3$ as well as free n parameters were attempted (Figure S20). The free n fit resulted in the closest value (0.877 ± 0.007) to the physically meaningful $n = 1$, which indicates 1D growth.[43,44] Indeed, the fit output and quality indicators for $n = 1$ differ minimally from those with the free n, while other fits $(n = 2$ or $3)$ deviate significantly from the experimental data (Figures S21, S22). The 1D growth is consistent with the rod-like morphology of Zn-MOF-74 materials established by further SEM experiments and XRD

results, and with the observations from the growth of rod crystals.[35] Therefore, $n = 1$ was used for the subsequent fits.

When P_N in eq 7 is combined with the information derived from ATR-IR spectroscopy and XRD, it becomes evident that the FWHM of the ATR-IR peak (Figure 4c) and P_N (Figure 4d) are strongly related (inset of Figure 4d). At the time of maximum nucleation (16 s), the broadest $\nu(C=C_{Ar})$ peak can be observed indicating that the system speciation was most diverse, containing uncoordinated and coordinated ligands as well as newly formed and grown nuclei. As the system evolved further, all parameters stabilized asymptotically at lower values. On the other hand, the appearance of the XRD peaks and the decrease of their FWHM started concomitantly with nucleation, confirming the rapid formation of the MOF phase as soon as the first nuclei became available. Once nucleation subsided, growth continued to yield the MOF with stabilized cell parameters (Figure 4b), vibrational spectrum (Figure 4a), and crystallite size and strain.

Synthesis with zinc perchlorate was also studied at 5 °C and exhibited similar behavior to that at 25 °C (Figure S19), albeit a slower evolution of XRD peak FWHM and lattice parameters as well as a short induction period of ca. 10−15 s where there was no MOF signal after mixing the reagents, which are likely associated with the low temperature. The FWHM of the $\nu(C=C_{Ar})$ peak strongly correlated with the probability of nucleation also at 5 °C, indicating the sensitivity of the ATR-IR peak width to the nucleation process over a broad temperature range (Figure S23)

In contrast to the perchlorate precursor, there was no noticeable dependence of XRD peak widths on Miller indices during synthesis with the zinc acetate (Figure S24a, b). The values of peak width were close to instrumental ones, indicating little sample contribution to peak broadening that was further corroborated by Williamson-Hall analysis (Figure S24c, d). This behavior suggests a larger crystallite size for the acetate-derived Zn-MOF-74 already from the early stages of synthesis.

Figure 5a shows the kinetic profiles of α for the synthesis experiments with zinc perchlorate at 5 and 25 °C and with zinc acetate at 25 °C. The 5-fold values of the kinetic constants of both nucleation (k_N) and growth $(k_G$, Figure 5b) suggest that at the same temperature, the synthesis with zinc perchlorate was faster. At 5 °C, k_N obtained with the zinc perchlorate precursor decreased nearly by a factor of 2, while k_G decreased only slightly, implying a higher activation energy for nucleation compared to growth, consistent with previous observations of MOF synthesis mechanisms.[23,44] Based on the tabulated values of parameter b in the Gualtieri model (Figure 5b), our data also reveal a change of nucleation mechanism from autocatalytic nucleation with zinc acetate to heterogeneous nucleation with zinc perchlorate.[43] We consider that this change of mechanism is related to the coordinating nature of the acetate ion. In zinc acetate, both acetate ions are chelated to the zinc ion, and two water molecules of hydration are attached to the zinc ion to form neutrally charged species (Figure 2b).[45] For zinc perchlorate solutions, the anion is not bound to zinc while zinc exists as $[Zn(H_2O)_6]^{2+}$ aqua ion (Figure 2a).[46] The ATR-IR spectrum of the aqueous solution of zinc perchlorate is thus characterized by the $\delta(O-H)$ mode of water bound to a charged ion at ca. 1620−1650 cm^{-1} despite the water solvent because zinc carries additional water.

Finally, the *in situ* data were supported by visual inspection of the MOF particles produced by the aqueous phase synthesis in various conditions using scanning electron microscopy (SEM,
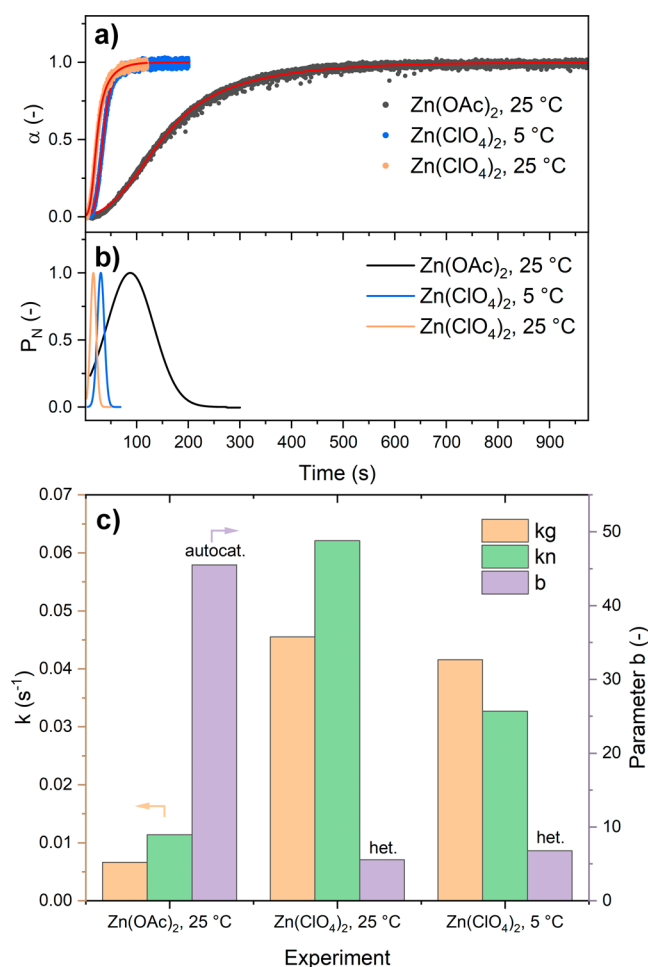
Figure 5. (a) Gualtieri fits and (b) Gualtieri model parameters for syntheses with zinc acetate and zinc perchlorate at 25 °C as well as zinc perchlorate at 5 °C. (c) Bar plots of kinetic parameters (k_N, nucleation constant, and k_G, growth constant) and b parameter from the Gualtieri model.

Figure 6), XRD, and BET surface area measurements by N_2 physisorption. Particle size distribution analysis of the images (Figures 6, 7ab, Figures S25, S26) revealed a clear dependence of particle shape parameters on the temperature of the perchlorate-based synthesis.

The particles produced at low temperatures (Figure 6ab) were rounder and more elongated toward rods with increasing temperature (Figure 6c−f). The longest particles belonged to the acetate-based synthesis (Figure 6g). Thus, particle length (Figure S26) and aspect ratio (Figure 7a) increased with increasing temperature, while the width remained within the same range in the two subgroups represented by the experiments at 5 and 10 °C and by those at higher temperatures (Figure 7b). This behavior was mirrored by the smaller values of the size of the XRD crystalline domain (Figures 7c, S27) and partly by the BET values (Figures 7d, S28, S29) in the syntheses performed at 5 and 10 °C. The FWHM and the position of the main ATR-IR peak of Zn-MOF-74 were also different for this group of temperatures (Figure S15). We propose that the different shape and size parameters for the particles obtained at low temperature were caused by a change of relation between k_N and k_G, with $k_G > k_N$ at low temperature and $k_G < k_N$ at high temperature. At low temperatures, the rate-limiting nucleation step allows only one way of nuclei evolution, which is growth from the solution,

resulting in numerous small particles as the pool of reactants in the solution promptly depletes after copious nucleation events. Such slow nucleation is corroborated by a clear induction period visible in the evolution of the $\nu(C=C_{Ar})$ peak FWHM and Gualtieri fit (Figure S23). At 10 °C, based on a lower BET area value and smaller XRD crystallite size of the product, it is postulated that the nucleation and growth constants do not significantly differ from each other, resulting in simultaneous nucleation and growth that create suboptimal conditions for the crystallization process. Inversely, growth is the rate-limiting step at high temperatures. Therefore, the nuclei can accumulate and evolve not only upon growth from the solution but also upon coalescence into larger nuclei or particles presumably within the (*ab*) plane. Only then they can grow along the *c* axis. This explains the large and relatively uniform particle width of the samples obtained above 10 °C.

Mechanism of Aqueous Phase Zn-MOF-74 Synthesis. The combination of the above information, obtained by *in situ* ATR-IR, high-energy XRD, and SEM, allows us to suggest a mechanism for the nucleation and growth of Zn-MOF-74 particles under the experimental conditions adopted here. In the case of zinc perchlorate, nucleation, as determined by Gualtieri fitting, is the rate-limiting step at low temperature (Figure 8a) and creates small nuclei. The faster growth process keeps the steady-state concentration of the nuclei low and their lifetime short, avoiding coalescence and producing numerous small, round particles. The round shape of the particles is dictated by a limited growth along the *c* axis (established by *in situ* XRD peak width and lattice analysis), as most of the reactants are consumed to form plentiful small nuclei. This is also in line with the submicron width of the product particles, which corresponds to the presumed width of nuclei, and a low aspect ratio of nearly one. At higher temperatures, crystal growth becomes the rate-limiting step. Hence, the nuclei are not immediately consumed by growth, their lifetime is long enough and the steady state concentration is relatively high (Figure 8b). Such high concentration of nuclei and longer lifetimes causes their coalescence (Ostwald ripening),[23,47] converting numerous small nuclei to a lower number of large nuclei, resulting in a relatively constant product particle width of ca. 2−3 μm at 20−40 °C, as determined by SEM. The coalesced nuclei grow along the *c* axis (*in situ* XRD results) to form elongated rod-like particles. We propose that the increase of the aspect ratio of particles with increasing temperature is influenced by the partial dissolution of small nuclei/MOF particles in these conditions, releasing zinc ions and the ligand into the solution and allowing larger crystals to grow longer. This recrystallization mechanism also explains the well-developed facets of the sample produced at 40 °C. At lower temperatures (20 and 25 °C), these effects are less pronounced, and the particles are shorter and only partially faceted.

Contrary to the perchlorate ion, the acetate ion is expected to act as an intrinsic modulator, competing with the ligand for zinc coordination sites, thus making both nucleation and growth processes reversible.[48] In such a set of conditions, both nucleation and growth are slower than with zinc perchlorate, and the type of nucleation is different, as evidenced by the Gualtieri fit results. However, because growth is still the rate-limiting step, nuclei coalescence might take place as indicated by the comparable particle width values to synthesis with zinc perchlorate at high temperatures. Slow nucleation and growth reduce the rate of consumption of the starting reagents, enabling
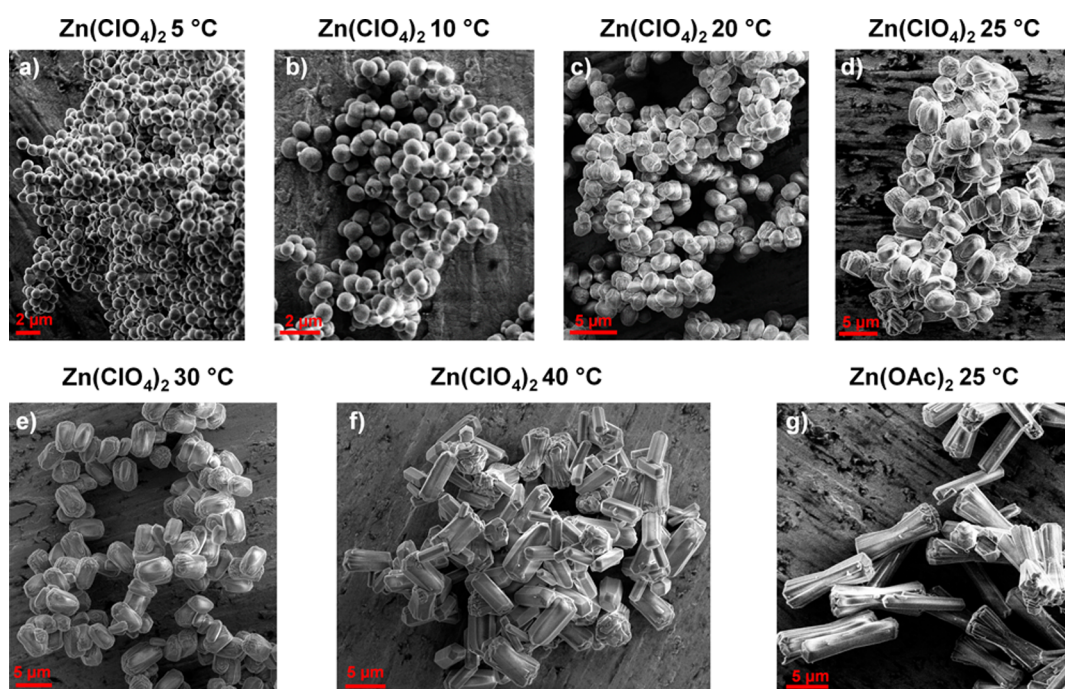
Figure 6. SEM images of Zn-MOF-74 particles synthesized under different conditions. (a) Zn(ClO$_4$)$_2$, 5 °C, (b) Zn(ClO$_4$)$_2$, 10 °C, (c) Zn(ClO$_4$)$_2$, 20 °C, (d) Zn(ClO$_4$)$_2$, 25 °C, (e) Zn(ClO$_4$)$_2$, 30 °C, (f) Zn(ClO$_4$)$_2$, 40 °C, (g) Zn(OAc)$_2$, 25 °C.
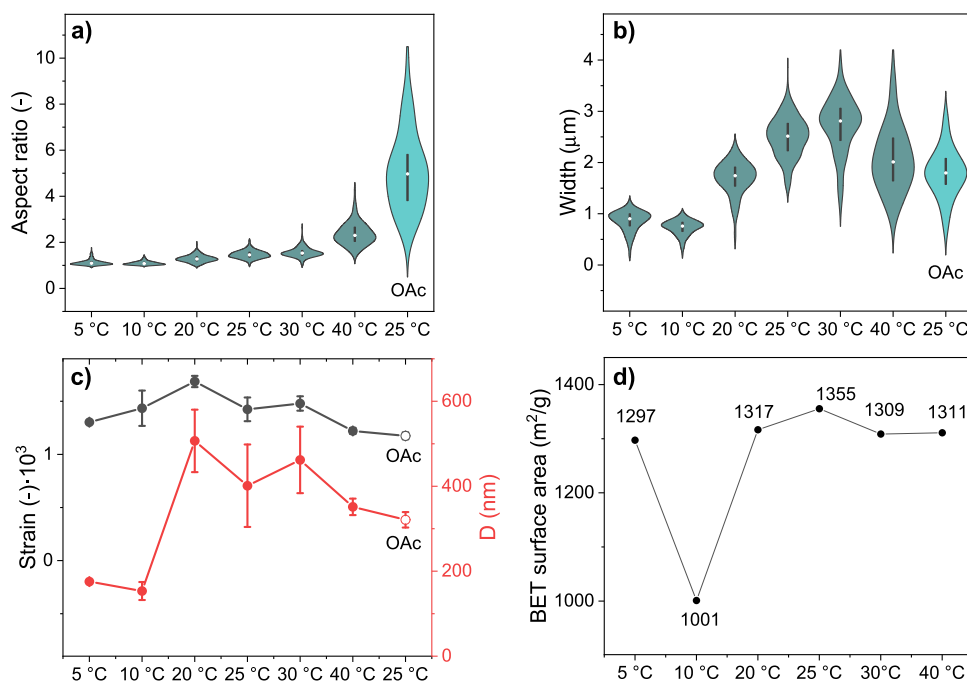

Figure 7. Violin plots of (a) aspect ratio and (b) width distributions, (c) strain and crystalline domain size according to Williamson-Hall analysis, and (d) BET surface areas, of Zn-MOF-74 products synthesized in different conditions. Error bars in (c) represent the estimated standard errors for the best-fit parameter values.

the few nuclei to grow into long rod-shaped particles (Figure 8c).

■ **CONCLUSIONS**

In this work, the combination of *in situ* ATR-IR and high-energy XRD enabled the elucidation of the mechanism of Zn-MOF-74 synthesis in the aqueous phase from zinc and ligand salts. A change of the zinc salt from acetate to perchlorate, initially motivated by the need for clarity of the infrared region of

interest, revealed that the kinetics of the synthesis depends strongly on the nature of the zinc salt used for the synthesis, as well as on reaction temperature. Observation of the nucleation process during the MOF synthesis was then possible through monitoring the evolution of the full width at half-maximum of the major characteristic $\nu(C{=}C_{Ar})$ MOF peak, which was corroborated by the results of Gualtieri model fitting of the analogous complementary *in situ* XRD data. The change in experimental protocol also allowed an improvement of the
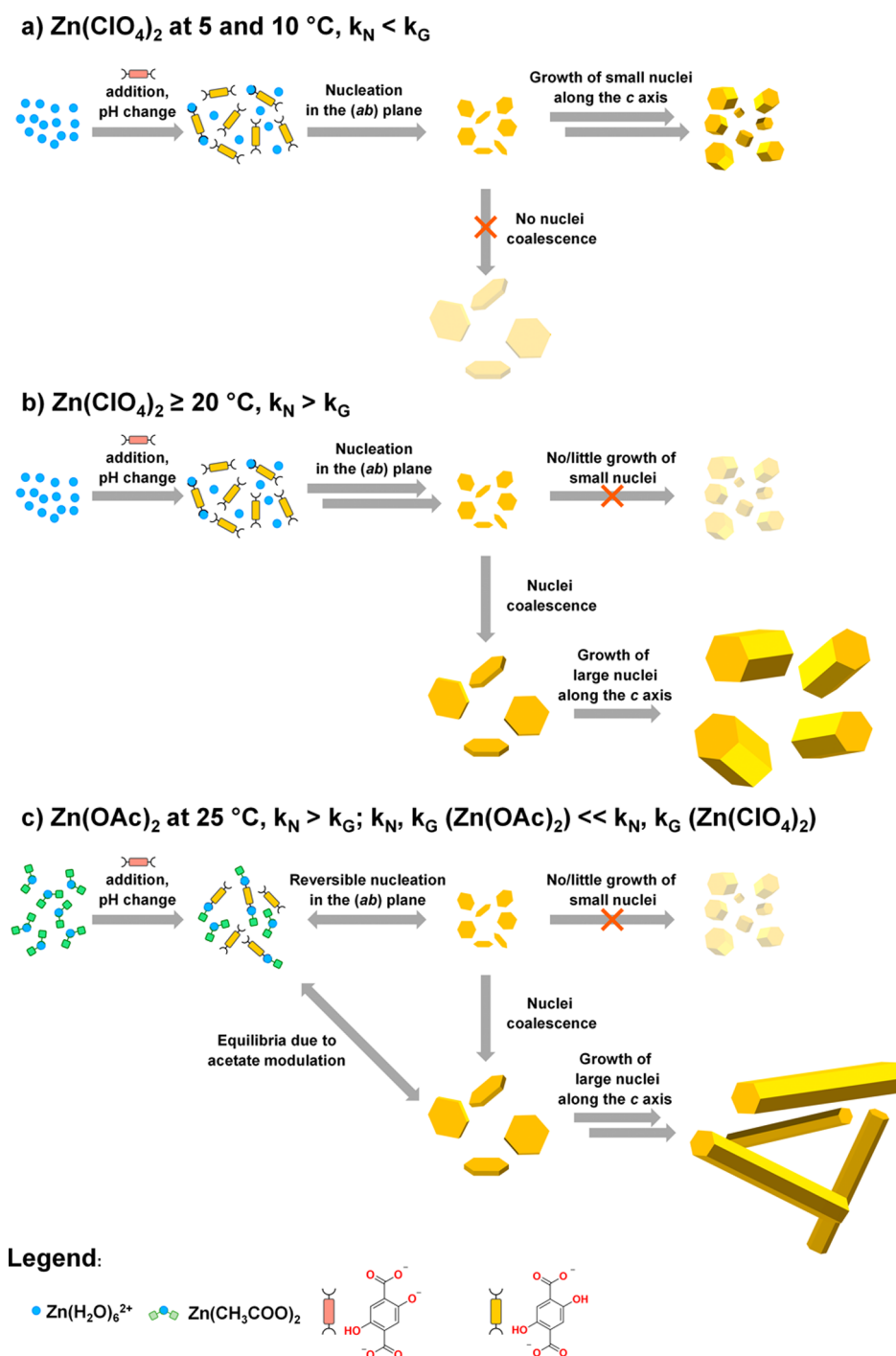
Figure 8. Suggested mechanism of Zn-MOF-74 synthesis (a) from $Zn(ClO_4)_2$ at 5 and 10 °C, (b) from $Zn(ClO_4)_2$ at ≥20 °C, (c) from $Zn(OAc)_2$ at 25 °C.

synthesis route and to obtain materials with controlled textural properties. Hence, *in situ* experimentation guided developments in materials synthesis. We demonstrated that the perchlorate-based synthesis was up to five times faster than the acetate-based synthesis and produced materials of comparable quality. The anisotropic growth of the MOF along the *c* axis in the hexagonal crystal system produced smaller particles and higher surface area MOF than the acetate-based synthesis. Such size- and shape-controlled MOF materials hold promise in applications like catalysis and separations, owing to their small, uniform particle size that enhances diffusion and separations within the MOF

pores. We believe that the understanding obtained in this work will lead to broader applicability of the aqueous synthesis route and its adaptation to other MOF families.

■ ASSOCIATED CONTENT

ⓈＩ Supporting Information

The Supporting Information is available free of charge at https://pubs.acs.org/doi/10.1021/acs.chemmater.4c00879.

> Schemes and images of experimental setups, reference IR spectra, raw IR and XRD data, raw data analysis results, SEM analysis particle count and distributions (PDF)

■ AUTHOR INFORMATION

Corresponding Authors

Ilia Kochetygov − *Paul Scherrer Institut, PSI Center for Energy and Environmental Sciences, Villigen PSI CH-5232, Switzerland;* ◉ orcid.org/0000-0001-8013-5885; Email: ilia.kochetygov@psi.ch

Davide Ferri − *Paul Scherrer Institut, PSI Center for Energy and Environmental Sciences, Villigen PSI CH-5232, Switzerland;* ◉ orcid.org/0000-0002-9354-5231; Email: davide.ferri@psi.ch

Authors

Luca Maggiulli − *Paul Scherrer Institut, PSI Center for Energy and Environmental Sciences, Villigen PSI CH-5232, Switzerland; Institute for Chemical and Bioengineering, ETH, Zurich, Zurich CH-8093, Switzerland;* ◉ orcid.org/0000-0001-5925-2817

Marco Ranocchiari − *Paul Scherrer Institut, PSI Center for Energy and Environmental Sciences, Villigen PSI CH-5232, Switzerland;* ◉ orcid.org/0000-0002-4460-8742

Complete contact information is available at:
https://pubs.acs.org/10.1021/acs.chemmater.4c00879

Notes

The authors declare no competing financial interest.

■ REFERENCES

(1) Furukawa, H.; Cordova, K. E.; O'Keeffe, M.; Yaghi, O. M. The Chemistry and Applications of Metal-Organic Frameworks. *Science* **2013**, *341* (6149), 1230444.

(2) Trickett, C. A.; Helal, A.; Al-Maythalony, B. A.; Yamani, Z. H.; Cordova, K. E.; Yaghi, O. M. The Chemistry of Metal−Organic Frameworks for CO₂ Capture, Regeneration and Conversion. *Nat. Rev. Mater.* **2017**, *2* (8), 17045.

(3) Sumida, K.; Rogow, D. L.; Mason, J. A.; McDonald, T. M.; Bloch, E. D.; Herm, Z. R.; Bae, T.-H.; Long, J. R. Carbon Dioxide Capture in Metal−Organic Frameworks. *Chem. Rev.* **2012**, *112* (2), 724−781.

(4) Murray, L. J.; Dincă, M.; Long, J. R. Hydrogen Storage in Metal−Organic Frameworks. *Chem. Soc. Rev.* **2009**, *38* (5), 1294−1314.

(5) Bauer, G.; Ongari, D.; Tiana, D.; Gäumann, P.; Rohrbach, T.; Pareras, G.; Tarik, M.; Smit, B.; Ranocchiari, M. Metal-Organic Frameworks as Kinetic Modulators for Branched Selectivity in Hydroformylation. *Nat. Commun.* **2020**, *11* (1), 1059.

(6) Gäumann, P.; Rohrbach, T.; Artiglia, L.; Ongari, D.; Smit, B.; van Bokhoven, J. A.; Ranocchiari, M. Tandem Hydroformylation-Aldol Condensation Reaction Enabled by Zn-MOF-74. *Chem.− Eur. J.* **2023**, *29* (38), No. e202300939.

(7) Woellner, M.; Hausdorf, S.; Klein, N.; Mueller, P.; Smith, M. W.; Kaskel, S. Adsorption and Detection of Hazardous Trace Gases by Metal−Organic Frameworks. *Adv. Mater.* **2018**, *30* (37), 1704679.

(8) Kalmutzki, M. J.; Hanikel, N.; Yaghi, O. M. Secondary Building Units as the Turning Point in the Development of the Reticular Chemistry of MOFs. *Sci. Adv.* **2018**, *4* (10), No. eaat9180.

(9) Kochetygov, I.; Roth, J.; Espín, J.; Pache, S.; Justin, A.; Schertenleib, T.; Taheri, N.; Chernyshov, D.; Queen, W. L. A Simple,

(10) Freund, R.; Zaremba, O.; Arnauts, G.; Ameloot, R.; Skorupskii, G.; Dincă, M.; Bavykina, A.; Gascon, J.; Ejsmont, A.; Goscianska, J.; et al. The Current Status of MOF and COF Applications. *Angew. Chem., Int. Ed.* **2021**, *60* (45), 23975−24001.

(11) Lin, J.-B.; Nguyen, T. T. T.; Vaidhyanathan, R.; Burner, J.; Taylor, J. M.; Durekova, H.; Akhtar, F.; Mah, R. K.; Ghaffari-Nik, O.; Marx, S.; et al. A Scalable Metal-Organic Framework as a Durable Physisorbent for Carbon Dioxide Capture. *Science* **2021**, *374* (6574), 1464−1469.

(12) Chakraborty, D.; Yurdusen, A.; Mouchaham, G.; Nouar, F.; Serre, C. Large-Scale Production of Metal−Organic Frameworks. *Adv. Funct. Mater.* **2023**, 2309089.

(13) Shi, Z.; Yuan, X.; Yan, Y.; Tang, Y.; Li, J.; Liang, H.; Tong, L.; Qiao, Z. Techno-Economic Analysis of Metal-Organic Frameworks for Adsorption Heat Pumps/Chillers: From Directional Computational Screening, Machine Learning to Experiment. *J. Mater. Chem. A* **2021**, *9* (12), 7656−7666.

(14) Anastasopoulou, A.; Furukawa, H.; Barnett, B. R.; Jiang, H. Z. H.; Long, J. R.; Breunig, H. M. Technoeconomic Analysis of Metal-Organic Frameworks for Bulk Hydrogen Transportation. *Energy Environ. Sci.* **2021**, *14* (3), 1083−1094.

(15) Subraveti, S. G.; Roussanaly, S.; Anantharaman, R.; Riboldi, L.; Rajendran, A. Techno-Economic Assessment of Optimised Vacuum Swing Adsorption for Post-Combustion CO₂ Capture from Steam-Methane Reformer Flue Gas. *Sep. Purif. Technol.* **2021**, *256* (October 2020), 117832−117832.

(16) DeSantis, D.; Mason, J. A.; James, B. D.; Houchins, C.; Long, J. R.; Veenstra, M. Techno-Economic Analysis of Metal−Organic Frameworks for Hydrogen and Natural Gas Storage. *Energy Fuels* **2017**, *31* (2), 2024−2032.

(17) Garzón-Tovar, L.; Carné-Sánchez, A.; Carbonell, C.; Imaz, I.; Maspoch, D. Optimised Room Temperature, Water-Based Synthesis of CPO-27-M Metal−Organic Frameworks with High Space-Time Yields. *J. Mater. Chem. A* **2015**, *3* (41), 20819−20826.

(18) Sánchez-Sánchez, M.; Getachew, N.; Díaz, K.; Díaz-García, M.; Chebude, Y.; Díaz, I. Synthesis of Metal−Organic Frameworks in Water at Room Temperature: Salts as Linker Sources. *Green Chem.* **2015**, *17* (3), 1500−1509.

(19) Tranchemontagne, D. J.; Hunt, J. R.; Yaghi, O. M. Room Temperature Synthesis of Metal-Organic Frameworks: MOF-5, MOF-74, MOF-177, MOF-199, and IRMOF-0. *Tetrahedron* **2008**, *64* (36), 8553−8557.

(20) Stock, N.; Biswas, S. Synthesis of Metal-Organic Frameworks (MOFs): Routes to Various MOF Topologies, Morphologies, and Composites. *Chem. Rev.* **2012**, *112* (2), 933−969.

(21) Kumar, S.; Jain, S.; Nehra, M.; Dilbaghi, N.; Marrazza, G.; Kim, K.-H. Green Synthesis of Metal−Organic Frameworks: A State-of-the-Art Review of Potential Environmental and Medical Applications. *Coord. Chem. Rev.* **2020**, *420*, 213407.

(22) Lee, Y.-R.; Kim, J.; Ahn, W.-S. Synthesis of Metal-Organic Frameworks: A Mini Review. *Korean J. Chem. Eng.* **2013**, *30* (9), 1667−1680.

(23) Salionov, D.; Semivrazhskaya, O. O.; Casati, N. P. M.; Ranocchiari, M.; Bjelić, S.; Verel, R.; van Bokhoven, J. A.; Sushkevich, V. L. Unraveling the Molecular Mechanism of MIL-53(Al) Crystallization. *Nat. Commun.* **2022**, *13* (1), 3762.

(24) Du Bois, D. R.; Wright, K. R.; Bellas, M. K.; Wiesner, N.; Matzger, A. J. Linker Deprotonation and Structural Evolution on the Pathway to MOF-74. *Inorg. Chem.* **2022**, *61* (11), 4550−4554.

(25) Cerasale, D. J.; Ward, D. C.; Easun, T. L. MOFs in the Time Domain. *Nat. Rev. Chem.* **2022**, *6* (1), 9−30.

(26) Julien, P. A.; Užarević, K.; Katsenis, A. D.; Kimber, S. A. J.; Wang, T.; Farha, O. K.; Zhang, Y.; Casaban, J.; Germann, L. S.; Etter, M.; et al. In Situ Monitoring and Mechanism of the Mechanochemical Formation of a Microporous MOF-74 Framework. *J. Am. Chem. Soc.* **2016**, *138* (9), 2929−2932.

(27) Weng, T.; Li, X.; Schmidt, J. R. In Situ, Time-Resolved, and Mechanistic Studies of Metal−Organic Framework Nucleation and Growth. *Chem. Rev.* **2018**, *118* (7), 3681−3721.

(28) Camp, C. H. J. Pymcr: A Python Library for Multivariate Curve Resolution Analysis with Alternating Regression (MCR-AR). *J. Res. Natl. Inst. Stand. Technol.* **2019**, *124*, 1−10.

(29) *Pybaselines: A Python Library of Algorithms for the Baseline Correction of Experimental Data*, 2022, https://zenodo.org/records/10676584.

(30) *Lmfit/Lmfit-Py: 2.1.* 2023. https://zenodo.org/record/7887568.

(31) Momma, K.; Izumi, F. Vesta 3 for Three-Dimensional Visualization of Crystal, Volumetric and Morphology Data. *J. Appl. Crystallogr.* **2011**, *44* (6), 1272−1276.

(32) Wong-Ng, W.; Kaduk, J. A.; Wu, H.; Suchomel, M. Synchrotron X-Ray Studies of Metal-Organic Framework M_2(2,5-Dihydroxyterephthalate), M = (Mn, Co, Ni, Zn) (MOF74). *Powder Diffr.* **2012**, *27*, 256−262.

(33) Schneider, C. A.; Rasband, W. S.; Eliceiri, K. W. NIH Image to ImageJ: 25 Years of Image Analysis. *Nat. Methods* **2012**, *9* (7), 671−675.

(34) Ferri, D.; Baiker, A. Advances in Infrared Spectroscopy of Catalytic Solid−Liquid Interfaces: The Case of Selective Alcohol Oxidation. *Top. Catal.* **2009**, *52* (10), 1323−1333.

(35) Panella, B.; Vargas, A.; Ferri, D.; Baiker, A. Chemical Availability and Reactivity of Functional Groups Grafted to Magnetic Nanoparticles Monitored in Situ by ATR-IR Spectroscopy. *Chem. Mater.* **2009**, *21* (18), 4316−4322.

(36) Tan, K.; Zuluaga, S.; Gong, Q.; Canepa, P.; Wang, H.; Li, J.; Chabal, Y. J.; Thonhauser, T. Water Reaction Mechanism in Metal Organic Frameworks with Coordinatively Unsaturated Metal Ions: MOF-74. *Chem. Mater.* **2014**, *26* (23), 6886−6895.

(37) de Juan, A.; Jaumot, J.; Tauler, R. Multivariate Curve Resolution (MCR). Solving the Mixture Analysis Problem. *Anal. Methods* **2014**, *6* (14), 4964−4976.

(38) Rosenthal, M. R. The Myth of the Non-Coordinating Anion. *J. Chem. Educ.* **1973**, *50* (5), 331.

(39) Max, J.-J.; Blois, S. D.; Veilleux, A.; Chapados, C. Ir Spectroscopy of Aqueous Alkali Halides. Factor Analysis. *Can. J. Chem.* **2001**, *79* (1), 13−21.

(40) Kornyshev, A. A.; Kuznetsov, A. M.; Spohr, E.; Ulstrup, J. Kinetics of Proton Transport in Water. *J. Phys. Chem. B* **2003**, *107* (15), 3351−3366.

(41) Mote, V. D.; Purushotham, Y.; Dole, B. N. Williamson-Hall Analysis in Estimation of Lattice Strain in Nanometer-Sized Zno Particles. *J. Theor. Appl. Phys.* **2012**, *6* (1), 6.

(42) Londoño-Restrepo, S. M.; Jeronimo-Cruz, R.; Millán-Malo, B. M.; Rivera-Muñoz, E. M.; Rodriguez-García, M. E. Effect of the Nano Crystal Size on the X-Ray Diffraction Patterns of Biogenic Hydroxyapatite from Human, Bovine, and Porcine Bones. *Sci. Rep.* **2019**, *9*, 5915. From NLM

(43) Gualtieri, A. F. Synthesis of Sodium Zeolites from a Natural Halloysite. *Phys. Chem. Miner.* **2001**, *28* (10), 719−728.

(44) Shearan, S. J. I.; Jacobsen, J.; Costantino, F.; D'Amato, R.; Novikov, D.; Stock, N.; Andreoli, E.; Taddei, M. In Situ X-Ray Diffraction Investigation of the Crystallisation of Perfluorinated Ce[IV]-Based Metal−Organic Frameworks with UiO-66 and MIL-140 Architectures**. *Chem.— Eur. J.* **2021**, *27* (21), 6579−6592.

(45) Sugimoto, K.; Kawaguchi, S.; Takemoto, M. Structural Characterization of Caffeine−Oxalic Acid Co-Crystals from the Powder Diffraction Pattern at the Spring-8 Bl02b2 Beamline. *Powder Diffr.* **2017**, *32*, S19−S26.

(46) Ghosh, S.; Mukherjee, M.; Seal, A.; Ray, S. X-Ray Study of $M^{II}(ClO_4)_2 \cdot 6H_2O$ (M^{II} = Zn, Ni): Twinning, Disorder and Phase Transitions. *Acta Crystallogr. B* **1997**, *53* (4), 639−644.

(47) Bonnett, B. L.; Ilic, S.; Flint, K.; Cai, M.; Yang, X.; Cornell, H. D.; Taylor, A.; Morris, A. J. Mechanistic Investigations into and Control of Anisotropic Metal−Organic Framework Growth. *Inorg. Chem.* **2021**, *60* (14), 10439−10450.

(48) Marshall, C. R.; Staudhammer, S. A.; Brozek, C. K. Size Control over Metal−Organic Framework Porous Nanocrystals. *Chem. Sci.* **2019**, *10* (41), 9396−9408.